Short Communication

Control of microstructure and shape memory properties of a Fe-Mn-Si-based shape memory alloy during laser powder bed fusion

I. Ferretto [a,b], A. Borzì [a], D. Kim [c], N.M. Della Ventura [a], E. Hosseini [a], W.J. Lee [d], C. Leinenbach [a,b,*]

[a] Empa, Swiss Federal Laboratories for Materials Science and Technology, 8600 Dübendorf, Switzerland
[b] École Polytechnique Fédérale de Lausanne (EPFL), Laboratory for Photonic Materials and Characterization, 1015 Lausanne, Switzerland
[c] Dongnam division, Korea Institute of Industrial Technology, 50623 Yangsan, Republic of Korea
[d] School of Material Science and Engineering, Pusan National University 2, Busandaehak-ro 63beon-gil, Geumjeong-gu, Busan 46241, Republic of Korea

ARTICLE INFO

ABSTRACT

Fe-Mn-Si shape memory alloys are materials, whose functional properties strongly depend on microstructural factors such as grain size and orientation, phase fraction and chemical composition. The present study demonstrates the possibility of microstructure modification via process parameter variation on a Fe-Mn-Si based shape memory alloy fabricated by laser powder bed fusion. By varying the scan speed, samples characterized by coarse elongated grains with strong <001> orientation along the build direction or by finer equiaxed grains without preferential orientation can be fabricated. Changes in the volume phase fraction of bcc-δ ferrite and fcc-γ austenite are also introduced by selective Mn evaporation. A direct correlation between the generated microstructure and achieved mechanical and shape memory properties is found.

Introduction

Fe-Mn-Si-based shape memory alloys (SMAs) are a class of smart materials that can recover the original shape after large deformation. The possibility of shape recovery is based on a mechanically induced martensitic transformation from fcc-γ austenite to hcp-ϵ martensite, and its reversion during unloading, i.e. pseudo-elasticity (PE), and during heating, i.e. shape memory effect (SME) [1]. Their shape memory properties are strongly influenced by the grain size and grain orientation [2].

In contrast to conventional manufacturing methods, additive manufacturing (AM) methods like laser powder bed fusion (LPBF) or electron beam melting (EBM) provide a unique way of fabricating complex geometries with almost no limitations in design, opening new prospective in several fields like biomedical, automotive, and aerospace [3]. AM of the most commonly used Ni-Ti-based SMAs has attracted significant attention in the last decades because of the excellent functional and mechanical properties of the alloys (such as low elastic anisotropy, mechanical strength, biocompatibility, corrosion resistance, enhanced shape memory properties) coupled with the increased freedom of design enabled by AM [4–8]. However, the high cost of raw material and the extreme sensitivity of functional properties on chemical composition represent the main drawbacks of this class of materials [9]. In this scenario, Fe-based alloys represent an attractive material option for AM of inexpensive structures made of SMAs [10]. In our previous studies

[11,12], complex functional parts showing enhanced SME have been successfully fabricated by LPBF from Fe-Mn-Si alloys.

By varying the laser (or electron beam) power and scan velocity, or the arc conditions in arc-based AM techniques, and by modifying the scan strategy, the thermal history in the deposited material can be significantly influenced, thereby enabling to manipulate the parts' microstructure and properties [13–15]. In this way, the crystallographic texture and grain size/morphology of several classes of alloys, e.g. stainless steels and Ni-alloys [16–19], could be successfully controlled during LPBF or EBM. Significant variations in grain size and texture have also been observed by modifying sample geometry, such as part dimensions and orientation, as heat flow direction, cooling rate, and temperature gradient are altered [10,20]. With regard to Fe-Mn-Si-based SMAs, the texture along the loading direction (LD) of Fe–17Mn–5Si–10Cr–4Ni SMA tensile samples fabricated by LPBF could be controlled by changing the sample orientation with respect to the build direction (BD) [11]. The preferred <101> orientation of austenite grains in the tensile samples built without inclination on the build plate (LD // BD) results in improved shape recovery exceeding the one of similar alloys but conventionally fabricated. The PE (ε_{pse}=1.18%) and SME (ε_{rec}=1.64%) for the LPBF-fabricated parts are more than 40% higher than for the conventionally fabricated samples, for which a maximum ε_{pse} of 0.8% and a maximum ε_{rec} of 1.15% have been achieved [9,21].

Several studies have been conducted in a range of metals to build spatially varying microstructures. As reported by Arabi-Hashemi et al.

---

* Corresponding author.
E-mail address: christian.leinenbach@empa.ch (C. Leinenbach).

Table 1

Chemical composition of the Fe-based SMA powder measured by wavelength dispersive X-ray fluorescence spectrometry (WD-XRF) and energy-dispersive X-ray spectroscopy (EDS);

Fe (wt.%)	Mn (wt.%)	Cr (wt.%)	Si (wt.%)	Ni (wt.%)	V (wt.%)	C (wt.%)
Bal.	17.7	10.1	4.5	4.3	0.7	0.2

[22], the use of a high volumetric energy density (VED) during LPBF of a high-nitrogen steel resulted in the selective evaporation of N and the stabilization of the ferromagnetic bcc phase at the expense of the paramagnetic fcc phase. The EBM fabrication of chemically graded parts has also been demonstrated for austenitic Cr-Mn-Ni transformation induced plasticity (TRIP) steels. A controlled Mn vaporization via adjustment of VED allows for the manufacturing of parts with distinct microstructure [23,24]. Mechanically tailored parts can thus be fabricated, with the possibility of modifying alloys' deformation and strengthening mechanisms.

In the present study, we demonstrate that the microstructure and thereby the thermo-mechanical properties of a Fe-Mn-Si-based SMA can be varied in a rather wide range by simply changing the laser scan velocity during LPBF. Samples characterized by highly textured columnar grains of austenite or by fine equiaxed microstructures consisting of austenite and ferrite grains without preferential orientation can be fabricated through selective evaporation of Mn and modification of the solidification conditions. Important variation in the parts' mechanical and shape memory properties are thus achieved.

Metamaterials and lattice structures made by Fe-SMAs seem to have considerable potential for the realization of new damping structures, which combine the damping capacity of SMAs with additional functionalities deriving from the parts' design and topology. In this way, new reusable structures for shock wave trapping, energy absorption and dissipation during impact, or vibration mitigation could be fabricated. In all these applications, structures are mainly subjected to compressive load. The investigation of the material's behavior during compression for different generated microstructures is thus rather important from an application point of view and will help for the design optimization of novel structural metamaterials and for the microstructure manipulation of the LPBF-fabricated parts.

Material and methods

Sample preparation

Gas atomized powder (Boehler Edelstahl, Kapfenberg, Austria) of a Fe–17Mn–5Si–10Cr–4Ni-1(V,C)-wt.% SMA was used for sample fabrication. The chemical composition provided in Table 1 is the average of the values obtained by energy-dispersive X-ray spectroscopy (EDS) analysis on a ground and polished powder using a scanning electron microscope (SEM) FEI NanoSEM 230 and by wavelength dispersive X-ray fluorescence spectrometry (WD-XRF) using a Rigaku Primus IV technique.

Bars with a length of 30 mm and thickness and width of 8 mm were fabricated from the powder by LPBF using the machine Sisma My Sint100. Three different scan velocities were applied for manufacturing. Sample S1 was fabricated with a laser scan velocity of $v_1 = 100$ mm/s, sample S2 with $v_2 = 250$ mm/s and sample S3 with $v_3 = 400$ mm/s. For all the samples, the laser power P_L was kept constant at 175 W. A layer thickness d of 30 μm and hatch spacing h of 100 μm, respectively, were selected. With these scan speeds, the resulting $VED = \frac{P_L}{v \cdot d \cdot h}$ is 583 J/mm^3, 233 J/mm^3, and 146 J/mm^3 for the S1, S2, and S3 samples, respectively.

The laser power and scan velocities have been chosen based on our previous work, where it was observed that a high VED (above 144 J/mm^3) is required to avoid defect and crack formation [11]. A maximum scan velocity of 400 mm/s was selected for the fabrication of the

samples, as in previous investigations the formation of lack of fusion defects was observed for higher speed. A bi-directional scan strategy with 90° rotation between the layers was applied.

Sample characterization

The cross section of the samples parallel to the BD was prepared for microstructure investigation by grinding with 600, 1200, 2500 and 4000 grit SiC paper and final polishing with 50 nm colloidal silica. Afterwards, the samples were etched using V2A etchant at room temperature (100 mL hydrochloric acid, 100 mL water, 10 mL nitric acid). A first analysis was performed by optical microscopy (OM) with a Zeiss Axiovert 100A/Canon DSLR. Further investigations were conducted by energy-dispersive X-ray spectroscopy (EDS) and electron back scatter diffraction (EBSD) using a (SEM) Tescan Mira equipped with an EDAX DigiView camera. The electron beam voltage was set to 20 kV, the step size was 1 μm for a 500 × 500 μm^2 map.

Complementary, X-ray diffraction (XRD) was applied using a PanAnalytical Empyrean equipped with a PixCel 3D detector using the Cu K$\alpha = 1.5418$ Å wavelength. Diffraction patterns were acquired in Bragg-Bentano geometry with angular range of 2θ from 30° to 130°. The texture of the samples was analyzed by performing the pole figures of the reflections of interest. The acquired data were analyzed by means of HighScore Plus [25] and X'Pert Texture software (Malvern PanAlytical). Background modeling and subtraction, peaks identification and fitting, and phase identification were performed on the HighScore Plus platform.

The chemical composition of the samples was analyzed by X-ray fluorescence spectroscopy (XRF) using a Thermo Scientific Niton XL5 Plus XRF Analyzer.

Thermo-mechanical characterization

The pseudo-elastic and shape memory behavior has been defined by compression test of cylindrical samples (h/d=1.5 [26,27]), as used for Ni-Ti-based [28–30] or Fe-Mn-Al-Ni-based [10] SMAs fabricated by LPBF. Cylindrical samples (5 mm diameter, 7.5 mm height, h/d=1.5) were machined for compression tests from the fabricated blocks such that the LD of the samples corresponds to the BD. Compression tests were performed using a Electromechanical Central Spindle testing machine [LFMZ-50-HM] equipped with a resistance furnace to characterize the samples' shape memory properties. In the first step, the samples were pre-strained to a strain of 2% and then unloaded with a deformation rate of 0.2 mm/min. From this first cycle, the pseudo-elastic behavior was characterized in terms of the pseudo-elastic strain, ε_{pse}. The PE values were obtained from the difference between the recovered strain associated with the linear elastic part of the deformation and the experimentally measured strain upon unloading. After unloading, the SME was activated by heating. The samples were heated up to 200°C and cooled down to room temperature (RT), at a rate of 2°C/min. The strain evolution was recorded during the entire thermal cycle with a side-entry extensometer. The final strain measured by the extensometer at 200°C and at the end of the thermal cycle was recorded as recovery strain ($\varepsilon_{rec,200°C}$ and $\varepsilon_{rec,RT}$).

Micro-hardness measurements were performed on the fabricated blocks using a Fischerscope HM2000 microhardness tester. A load of 300 mN was applied for 10 s. An average value was calculated from 9 measurements in different positions of the samples.
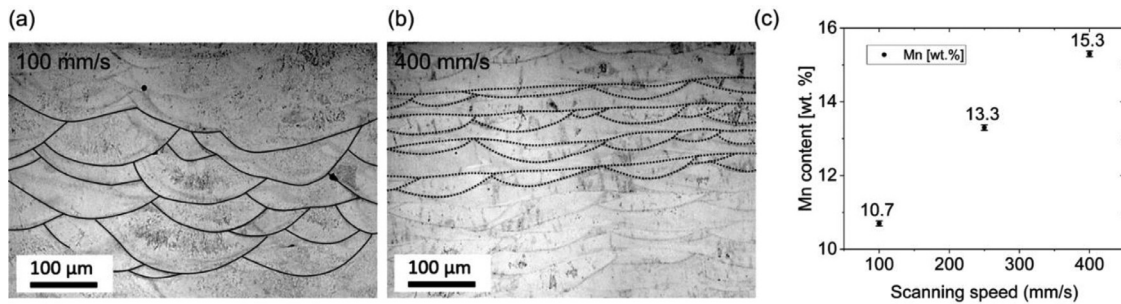
Fig. 1. Optical microscope images showing melt pool size and morphology in the samples fabricated with 100 mm/s (S1) (a) and 400 mm/s (S3) (b) scan speed; variation in the amount of Mn with the applied scan speed (c);

Results and discussion

Microstructure formation

Fig. 1 shows the optical images of the polished and etched surfaces of the samples S1 and S3. Melt pool boundaries are highlighted by black lines.

When the lowest speed of 100 mm/s is applied (S1), deep melt pools form (Fig. 1-a). A decrease in the scan speed causes longer lifetimes of the melt pool and higher maximum temperatures of the liquid phase, as the heat input is drastically increased and the heat transfer from the molten pool requires longer time. This results in larger and deeper melt pools, which overlap [22]. The dissipation of heat from the melt pool causes a curved melt pool shape. Melt pools are much deeper than the layer thickness (30 μm), indicating that most of the already solidified materials is re-melted during deposition of the top layers. The high depth of the melt pools observed at low scan speed might be also ascribed to the fact that most of the heat of the melt adjacent to the powder is transferred to the dense, solidified alloy below, which is characterized by a higher thermal conductivity than the powder [31].

At a higher speed of 400 mm/s (S3), melt pools become elongated but shallower and flatter (Fig. 1-b). Because of the lower heat introduced with the increasing speed, heat is quickly dissipated, resulting in melt pools with reduced dimensions. The bottom of the melt pools is nearly horizontally oriented because of the high scan speed [32]. With the lower heat input two differently oriented melt pool boundaries are clearly identified, one created along the cross-section and one normal to the cross-section, as expected for the 90° scan rotation. The melt pools are fairly aligned with the melt pools underneath.

According to XRF measurements, important variation in the amount of Mn in the as-built samples is also observed with the change in the scan speed. The Mn content in the samples reduces with decreasing scan speed, presumably due to evaporation (Fig. 1-c). Evidence of Mn evaporation during the process has been already observed in [23] and is ascribed to the high vapor pressure of this element in the melt [33]. As a decrease in the scan speed leads to higher maximum temperature of the liquid phase [22] and results in formation of deeper melt pools with longer lifetime and pronounced overlapping, the loss in Mn is more pronounced in S1, where an almost 5 wt.% lower amount of Mn (10.7% ± 0.069) is detected compared to S3 (15.3% ± 0.077), and in S2 (13.3% ± 0.074). No significant differences in the amount of the other elements are observed among the chemical compositions of the samples (Table A 1 in Appendix A).

The EBSD data for the samples fabricated with different scan speed (S1, S2, S3) are compared in Fig. 2.

At low and intermediate scan speed (100 and 250 mm/s), finer austenite grains (average diameter of 13 and 9 μm, respectively) with a very weak <111> or <101> preferential orientation along the BD form (Fig. 2-b,c,e,f). Some regions characterized by more elongated austenite grains with a length of ~20-30 μm are observed. At the higher scan speed of 400 mm/s (Fig. 2-h,i), the austenite grains are elongated along

the BD with a preferential alignment along the <001> direction, generating a <001> texture. Grains are coarser with a high aspect ratio compared to the previous cases. The average grain size of the austenite grains increases to 34 μm in S3.

A significant change in the phase fraction is also noted according to the EBSD maps with phase coloring. While S3 shows an almost fully austenitic microstructure (less than 1% bcc-δ), the volume fraction of ferrite increases with a reduction in the scan speed, with the highest amount for S1 (more than 12% bcc-δ) and a <101> texture along the BD. Similar ferrite content is observed for S2 (12%), with a preferential <001> orientation along the BD. A limited amount of hcp-ε martensite (<2%) is observed in S1. The amount of hcp-ε is less than 0.5% for S2 and S3.

The XRD patterns are reported in Fig. 3-a, showing the diffraction peaks of fcc-γ austenite and bcc-δ ferrite. Additional peaks at low intensity appear in the sample fabricated with the lowest speed (Fig. 3-b) and indicate the presence of Cr-rich precipitates with a fcc structure [34]. XRD patterns of S2 and S3 do not show these phases, pointing out their formation being limited or prevented with increasing scan velocity. Peaks related to the hcp-ε are not detected by XRD, probably due to the very low concentration of this phase.

The texture evolution of the samples is confirmed by the pole figure measurements reported in Fig. 3-c. The sample fabricated with the lowest scan speed (S1) shows an almost random texture (maximum texture indices of 2.3), with the 020 reflection of the austenite phase partially oriented in the out-of-plane direction, i.e. along the BD, and at an angle of 55˚, which indicates a preferential orientation of <111> along the BD. A weak texture along the BD is also observed for S2, whereas the sample fabricated with the highest scan speed shows a strong <001> texture (maximum texture indices of 10.5).

The important variation in the microstructure detected by EBSD and XRD is ascribed to the change in the chemical composition of the alloy, as well as to the varying heating and cooling conditions resulting from the different scan velocities. The pronounced loss in Mn due to evaporation significantly affects phase stability and the primary solidification mode. In Fe-Mn-Si-Cr-Ni alloys, the ratio between ferrite stabilizing elements, defined by the chromium equivalent ($Cr_{eq} = Cr + 1.5Si$), and austenite stabilizing elements, nickel equivalent ($Ni_{eq} = Ni + 0.31Mn + 22C$), gives an indication of the primary phase, which forms during solidification [35]. For a ratio below 1.5, austenite is supposed to be the primary solidification phase. According to these empirical rules, the formation of austenite as primary phase is promoted in S3, characterized by the highest amount of the austenite stabilizer Mn (15.3 wt.%) and the lowest ratio Ni_{eq}/Cr_{eq} (1.3). The grain morphology and the orientation of the austenite grains provide evidence of austenite as primary phase in S3. Austenite solidifies as columnar grains elongated along the BD with a preferred <001> orientation, as generally observed in most cubic alloys fabricated by PBF at comparably fast scan speed [32]. The formation of a pronounced crystallographic texture and large grains derives from the epitaxial grain growth [36]. Previously deposited layers are partially re-melted and grow preferentially with the
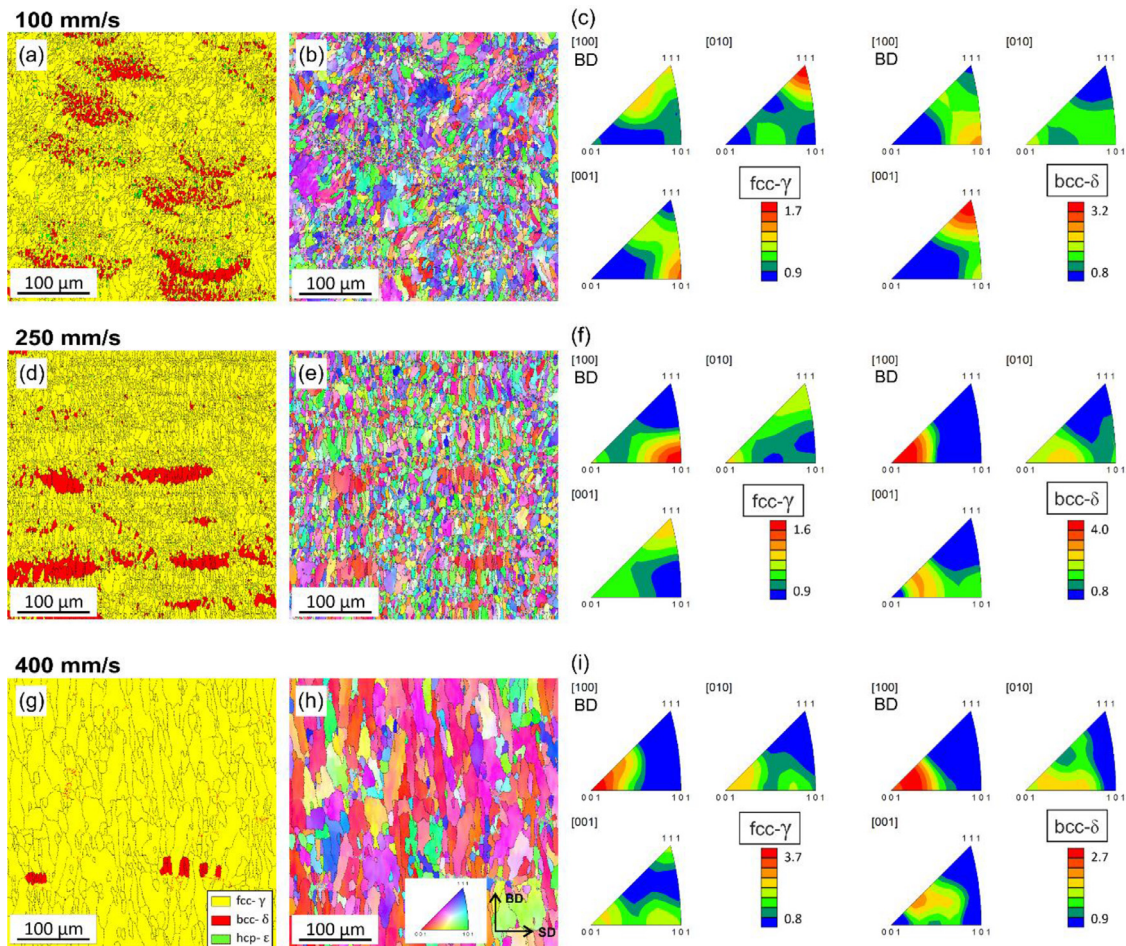
Fig. 2. Electron back scatter diffraction (EBSD) maps with phase coloring for the samples fabricated with 100 mm/s (a), 250 mm/s (d) and 400 mm/s (g) scan speed; EBSD maps with inverse pole figure (IPF) coloring and IPFs for the samples fabricated with 100 mm/s (b-c), 250 mm/s (e-f) and 400 mm/s (h-i) scan speed;

<001> direction parallel to the maximum heat gradient, i.e. perpendicular to the local curvature of the melt pool boundary. Considering the nearly horizontally oriented bottom of the melt pools, a strong <001> texture develops along the BD.

Differently from S3, a superior volume fraction of the bcc-δ phase is observed for S1 and S2. Due to the lower amount of the austenite stabilizer Mn in these samples, the formation of bcc-δ as primary phase is favored compared to the previous sample, increasing the amount of the ferrite in S1 and S2. This is in line with previous investigations on AM-manufactured and conventionally fabricated CrMnNi steels, which report increased bcc-δ fractions with increased depletion of Mn [24,37,38]. The <101> texture of the primary ferrite in sample S1 is ascribed to the curvature at melt pools' trailing edge and to the so called side-branching effect [13]. Beside <001>, the generation of <101> texture has been observed upon solidification for both fcc and bcc when a high VED and bi-direction scanning strategy with 90° rotation are applied [13].

The thermal history experienced by the material during LPBF is particularly complex. The layer-wise additive manufacturing induces an intrinsic heat treatment (re-heating) on the already solidified material during deposition. Previous TEM investigations on a similar alloy fabricated by LPBF show that this re-heating effect is responsible for a solid-state phase transformation of the primary bcc-δ to fcc-γ in the bottom layers [39]. At lower scan speeds (i.e. in samples S1 and S2), a high amount of heat is transferred to the pre-deposited layers. This reduces the cooling rate and increases the time for the solid-state bcc-δ → fcc-γ transformation to occur [40]. It can be thus assumed that the primary bcc-δ partially transforms to fcc-γ during deposition.

The TEM results in the previous study have indicated a Kurdjumov and Sachs (K-S) orientation relationship (OR) between the bcc-δ and fcc-γ phases when the fcc-γ is transformed from the bcc-δ during the LPBF process [20]. The 020 reflection of the austenite phase partially oriented around 55° observed from the pole figure analysis confirms a solid state transformation in S1, as the fcc-γ phase inherits the texture from the primary bcc-δ phase following closely the semicoherent K-S OR with {111}γ // {011}δ. The coherent K-S OR is observed for S2, leading to the weak <101> texture of the austenite grains along the BD from the <001> oriented ferrite grains [39]. The weak texture of the fcc-γ phase with 020 reflections at 55° as well as along the BD of S1 and S2 can be ascribed to the fact that austenite can form as both primary phase and secondary phase from the phase transformation. Indeed, local alterations of the alloy's chemical composition are caused by distinct Mn evaporation, precipitation and segregations. According to SEM-EDS maps (Fig. A 1 in Appendix A) the amount of Mn ranges from 10 wt.% to 16.7 wt.% in different locations of sample S1 because of the distinct evaporation within the melt pool caused by the complex thermal history and temperature distribution experienced by the sample. The distribution of the other elements is more homogenous. Some regions slightly enriched in Si (5.8 wt.%) or Cr (12.4 wt.%) are observed, probably due to segregation [41]. Varying cooling conditions within the melt pools are also expected, locally affecting the solidification behavior of the alloy.

Based on the variation in texture and grain size between the samples, it can be stated that the formation of ferrite as primary phase associated with Mn evaporation at low scan speeds and its partial transformation during deposition refine the microstructure and prevent preferen-
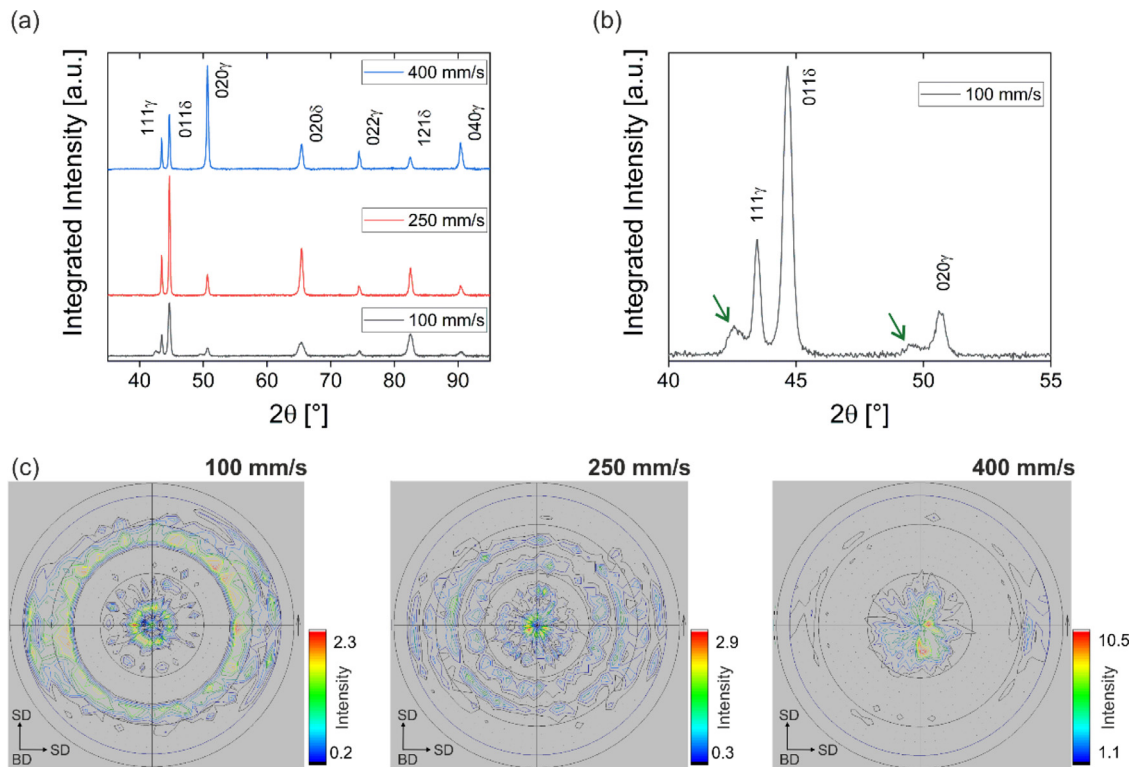
Fig. 3. X-ray diffraction (XRD) patterns obtained with the diffraction vector parallel to the built direction for the samples fabricated with 100 mm/s (black), 250 mm/s (red) and 400 mm/s (blue) scan speed (a); details of the XRD pattern for the sample fabricated with 100 mm/s scan speed, indicating the presence of precipitates (green arrows) (b); pole figures for the 020γ reflection of the samples fabricated with different scan speed (c);

tial grain orientation of austenite, explaining the duplex microstructure ($\sim$12% bcc-δ) with fine austenite grains and low texture intensity of S1 and S2 samples [24,36]. The retained bcc-δ might be the result of local compositional differences and the spatially varying temperature fields in the samples. The formation of columnar grains with preferential crystallographic orientation, which normally results in strong anisotropy in the mechanical properties of LPBF fabricated parts, can be suppressed by reducing the scan speed. Interestingly, an opposite trend than what is typically observed during LPBF is found, considering that the use of lower scan speeds normally results in grain growth and strong texture along the BD [42].

The pronounced re-heating and reduced cooling rate achieved at low scan speed also induce the formation of precipitates. In situ precipitation during LPBF has been already observed in different alloys, e.g. maraging steels, nickel-base superalloys and scandium-containing aluminum alloys [43,44]. It is known that precipitation mainly occurs by re-melting and by intrinsic heat treatment during the deposition of the top layers. Precipitates might also form during cooling from the liquid state after deposition, but only for slow cooling rate [43]. The presence of precipitates might be the reason of hcp-ε martensite formation prior mechanically loading. Internal stress arises around the particles because of thermal expansion and lattice mismatch with the matrix [21].

Mechanical and shape memory properties

The distinct microstructures resulting from the application of different scan speeds lead to important variation in the samples' mechanical and shape memory performance. Table 2 summarizes the main properties measured from compression and hardness tests.

In comparison to the samples S2 and S3, for which hardness values of 360 and 343 HV, respectively, are measured, an increased hardness is observed for S1. For the later, a maximum value of 419 HV is achieved, which is significantly higher than the hardness (356 HV) measured for

the same alloy but conventionally fabricated by hot forging and heat treated (solution treatment and aging at 800°C, 2h) [9,21,45]. Fig. 4 shows the stress-strain curves obtained from the compression tests of the three samples. The highest strength is observed for the S1 sample, followed by S2 and S3. The stress achieved at 2% strain is defined as $\sigma_{2\%}$ in Fig. 4-a,b,c. At 2% strain, a stress of 1131 MPa is reached for S1, which is 376 MPa higher than S3 ($\sigma_{2\%}$ = 755 MPa). An intermediate value of 873 MPa is measured for S2.

By comparing the stress-strain curves of the samples, it is noticed that the pseudo-elastic behavior strongly reduces for S1, showing the lowest ε_{pse}, 0.17%, among the three samples. Despite the final strain recovered upon unloading is higher for S1 compared to S3, only 18% of the recovered strain in S1 is related to the pseudo-elastic behavior of the material, the rest is related to the linear elastic strain recovery. For the sample fabricated with the highest scan velocity, S3, an inferior linear elastic recovery is observed due to the inferior strength of the sample, but more than 30% of the total recovered strain is pseudo-elastic, with a ε_{pse} of 0.21%.

Fig. 4-d,e,f shows the strain evolution during the thermal cycle. In the first stage, i.e. during heating to 200°C, the samples expand and tensile strains are recorded. The measured tensile strain arises from the thermal expansion of the samples and from the strain recovery associated with the SME activated by heating. In the second stage, cooling to RT, tensile strain reduces due to samples' thermal contraction. A higher tensile strain is achieved at 200°C ($\varepsilon_{rec,200°C}$) for S3, 0.80%, compared to S1 and S2 (0.50%, 0.72%), indicating a more pronounced SME for the former. The total strain recovery after the whole heating-cooling cycle, i.e. $\varepsilon_{rec,RT}$, is more than three times higher for S3 (0.39%) compared to S1 (0.12%).

The variation in mechanical and shape memory properties observed for the samples can be ascribed to the different generated microstructures. The higher strength and hardness for lower scan speeds of 100 mm/s and 250 mm/s are the result of the larger amount of bcc-δ, which

Table 2

Mechanical and shape memory properties for the samples fabricated with different scan speed;

	Hardness [HV]	$\sigma_{2\%}$ [MPa]	ε_{pse} [%]	ε_{elast} [%]	$\varepsilon_{pse}/\varepsilon_{elast}$ x100 [%]	$\varepsilon_{rec,\ 200°C}$ [%]	$\varepsilon_{rec,RT}$ [%]
S1	419 ± 17	1131	0.17	0.92	18	0.50	0.12
S2	360 ± 14	873	0.25	0.97	26	0.72	0.28
S3	343 ± 12	755	0.21	0.69	30	0.80	0.39
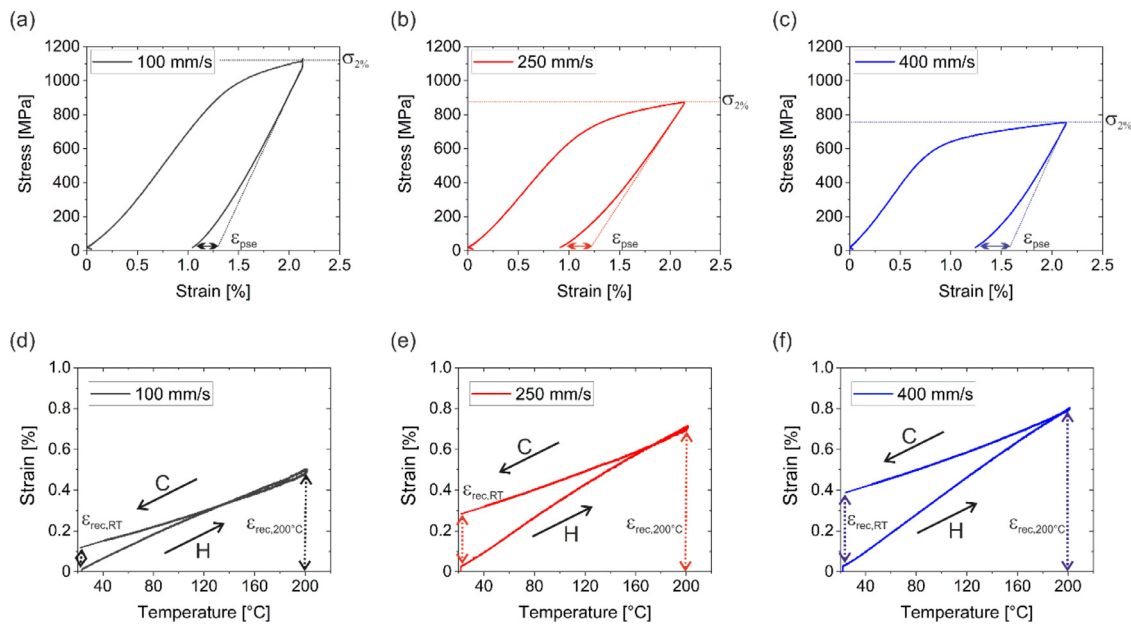
Fig. 4. Stress-strain curves during compression tests for the samples fabricated with 100 mm/s (a), 250 mm/s (b) and 400 mm/s (c) scan speed and evolution of strain with heating up to 200°C (H) and cooling (C) to room temperature for the samples fabricated with 100 mm/s (d), 250 mm/s (e) and 400 mm/s (f) scan speed;

is generally harder than austenite [46,47], and of the finer microstructure [48]. The formation of precipitates in S1 also contribute to increase sample's hardness and strength [49,50].

The larger amount of ferrite formed at low scan speed also leads to a decrease in PE and SME. The strain recovery of the alloy is caused by the reverse transformation of hcp-ε to fcc-γ during unloading and/or heating. Larger strain recovery indicates a more pronounced martensite formation during deformation, which can then transform back to austenite. As hcp-ε forms from extension and overlap of stacking faults (SFs) in the fcc-γ austenite lattice during deformation [51,52], the presence of bcc-δ ferrite reduces the possibility of martensite formation in S1 and S2 compared to S3. Additionally, the high amount of precipitates in S1 might also negatively affect the shape memory properties by blocking the movement of Shockley partial dislocations, thus increasing the critical stress for stress-induced martensite formation [53]. For this reason, controlled precipitation (in terms of size and density of precipitates) by aging treatment is required for the present alloy to improve the material's SME and PE.

A higher amount of martensite is expected to form in S3 as a consequence of the austenite texture along the LD. Considering that fcc-γ → hcp-ε is a shear transformation with an underlying (111)<112> shear system and that the <001> direction has a high Schmid factor of 0.47 [2], pronounced martensitic transformation is expected in S3 due to the high amount of {001} grains preferentially oriented along the LD [54]. Other important factors, which might have a certain impact on the extent of the martensite transformation are stacking fault energy [55] and transformation temperatures [56], which, in turn, directly depend on the chemical composition. Further investigations will be performed in this regard.

The present work shows the possibility of microstructure and property manipulation of Fe-Mn-Si-based SMAs offered by LPBF. Adjusting

the VED by simply varying the scan speed leads to significant changes of the microstructure, as well as of the deformation and shape memory behavior of the material. Understanding the fundamentals of the process-microstructure-property relationships governing the Fe-Mn-Si-based alloys manufactured via LPBF is one step towards the fabrication of graded materials with site-specific properties, which can be tuned according to the intended application. By simply modifying the laser parameters, distinct microstructure could be integrated in a single component to fabricate graded structures that incorporate different properties and multiple functionalities. The control of Mn evaporation and the change in the thermal history experienced by the sample can be efficiently used for this scope. The approach of alloy's composition control by changing the scan speed can be extended to other classes of alloys containing volatile elements, such as Al, N, and Mn [57].

Conclusions

In the present study, the possibility of microstructure and property manipulation for a Fe-Mn-Si-based SMA by varying the laser scan velocity during LPBF was investigated. The following conclusions can be made:

1. Important variations in grain size, morphology and orientation, as well as in phase fraction of bcc-δ and fcc-γ can be induced if the scan velocity increases from 100 mm/s to 400 mm/s.
2. The reasons of the distinct microstructure are found in the distinct evaporation of Mn in the samples, which affects the primary solidification phase formation from fcc-γ to bcc-δ, and in the effect of the intrinsic heat treatment, which causes the solid-solid phase transformation bcc-δ → fcc-γ during cooling.
3. A clear correlation between the microstructure and the mechanical/shape memory properties is found, indicating the possibility of property tailoring in 3D parts via processing parameters.

Table A1

Chemical composition of the as-built samples (S1, S2, S3) measured by X-ray fluorescence spectroscopy (XRF);

Sample	Scan speed (mm/s)	Fe (wt.%)	Mn (wt.%)	Cr (wt.%)	Si (wt.%)	Ni (wt.%)	V (wt.%)	C (wt.%)
S1	100	bal.	10.7	10.4	6	4.6	0.7	0.2
S2	250	bal.	13.3	10.3	5.7	4.4	0.7	0.2
S3	400	bal.	15.3	10.1	5.5	4.2	0.7	0.2

Declaration of Competing Interest

The authors declare that they have no known competing financial interests or personal relationships that could have appeared to influence the work reported in this paper.

CRediT authorship contribution statement

I. Ferretto: Conceptualization, Methodology, Validation, Investigation, Data curation, Visualization, Writing – original draft. **A. Borzì:** Validation, Methodology, Investigation, Data curation, Writing – review & editing. **D. Kim:** Validation, Investigation. **N.M. Della Ventura:** Validation, Investigation, Writing – review & editing. **E. Hosseini:** Validation, Writing – review & editing. **W.J. Lee:** Conceptualization, Writing – review & editing, Supervision. **C. Leinenbach:** Conceptualization, Writing – review & editing, Project administration, Supervision.

Acknowledgment

Appendix

Table A1, Fig. A1
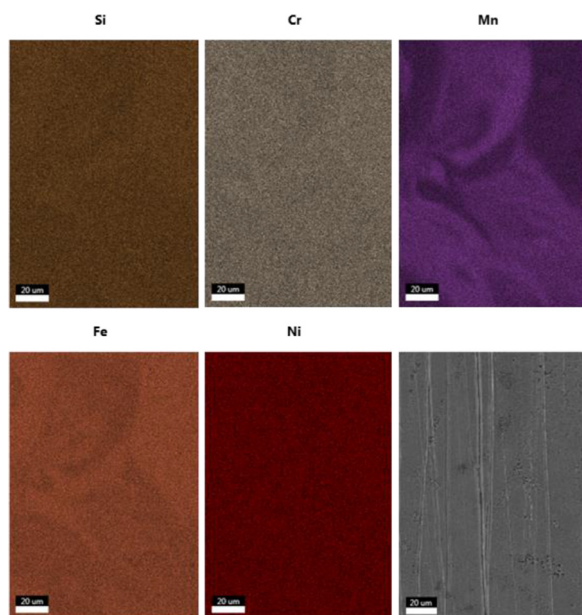
Fig. A1. Energy-dispersive X-ray spectroscopy (EDS) maps of S1 sample;

Supplementary materials

Supplementary material associated with this article can be found, in the online version, at doi:10.1016/j.addlet.2022.100091.

References

[1] A. Collazo, R. Figueroa, C. Mariño-Martínez, C. Pérez, Microstructure and thermomechanical characterization of Fe-28Mn-6Si-5Cr shape memory alloy, Metals 11 (2021) 649, doi:10.3390/met11040649.

[2] A. Arabi-Hashemi, E. Polatidis, M. Smid, T. Panzner, C. Leinenbach, Grain orientation dependence of the forward and reverse fcc ↔ hcp transformation in FeMnSi-based shape memory alloys studied by in situ neutron diffraction, Mater. Sci. Eng.: A 782 (2020) 139261, doi:10.1016/j.msea.2020.139261.

[3] L. Constantin, N. Kraiem, Z. Wu, B. Cui, J.-L. Battaglia, C. Garnier, J.-F. Silvain, Y.F. Lu, Manufacturing of complex diamond-based composite structures via laser powder-bed fusion, Addit. Manuf. 40 (2021) 101927, doi:10.1016/j.addma.2021.101927.

[4] J. Shen, Z. Zeng, M. Nematollahi, N. Schell, E. Maawad, R.N. Vasin, K. Safaei, B. Poorganji, M. Elahinia, J.P. Oliveira, In-situ synchrotron X-ray diffraction analysis of the elastic behaviour of martensite and H-phase in a NiTiHf high temperature shape memory alloy fabricated by laser powder bed fusion, Addit. Manuf. Lett. 1 (2021) 100003, doi:10.1016/j.addlet.2021.100003.

[5] B. Li, L. Wang, B. Wang, D. Li, J.P. Oliveira, R. Cui, J. Yu, L. Luo, R. Chen, Y. Su, J. Guo, H. Fu, Tuning the microstructure, martensitic transformation and superelastic properties of EBF3-fabricated NiTi shape memory alloy using interlayer remelting, Mater. Des. 220 (2022) 110886, doi:10.1016/j.matdes.2022.110886.

[6] M. Elahinia, N. Shayesteh Moghaddam, M. Taheri Andani, A. Amerinatanzi, B.A. Bimber, R.F. Hamilton, Fabrication of NiTi through additive manufacturing: a review, Prog. Mater. Sci. 83 (2016) 630–663, doi:10.1016/j.pmatsci.2016.08.001.

[7] Q. Zhang, S. Hao, Y. Liu, Z. Xiong, W. Guo, Y. Yang, Y. Ren, L. Cui, L. Ren, Z. Zhang, The microstructure of a selective laser melting (SLM)-fabricated NiTi shape memory alloy with superior tensile property and shape memory recoverability, Appl. Mater. Today 19 (2020) 100547, doi:10.1016/j.apmt.2019.100547.

[8] B. Li, L. Wang, B. Wang, D. Li, J.P. Oliveira, R. Cui, J. Yu, L. Luo, R. Chen, Y. Su, J. Guo, H. Fu, Electron beam freeform fabrication of NiTi shape memory alloys: Crystallography, martensitic transformation, and functional response, Mater. Sci. Eng.: A 843 (2022) 143135, doi:10.1016/j.msea.2022.143135.

[9] M. Koster, W.J. Lee, M. Schwarzenberger, C. Leinenbach, Cyclic deformation and structural fatigue behavior of an FE–Mn–Si shape memory alloy, Mater. Sci. Eng.: A 637 (2015) 29–39, doi:10.1016/j.msea.2015.04.028.

[10] T. Niendorf, F. Brenne, P. Krooß, M. Vollmer, J. Günther, D. Schwarze, H. Biermann, Microstructural Evolution and Functional Properties of Fe-Mn-Al-Ni Shape Memory Alloy Processed by Selective Laser Melting, Metall. Mater. Trans. A 47 (2016) 2569–2573, doi:10.1007/s11661-016-3412-z.

[11] I. Ferretto, D. Kim, N.M. Della Ventura, M. Shahverdi, W. Lee, C. Leinenbach, Laser powder bed fusion of a Fe–Mn–Si shape memory alloy, Addit. Manuf. 46 (2021) 102071, doi:10.1016/j.addma.2021.102071.

[12] D. Kim, I. Ferretto, C. Leinenbach, W. Lee, 3D and 4D Printing of Complex Structures of Fe·Mn·Si-Based Shape Memory Alloy Using Laser Powder Bed Fusion, Adv. Mater. Interfaces n/a (n.d) (2022) 2200171, doi:10.1002/admi.202200171.

[13] M.-S. Pham, B. Dovgyy, P.A. Hooper, C.M. Gourlay, A. Piglione, The role of side-branching in microstructure development in laser powder-bed fusion, Nat. Commun. 11 (2020) 749, doi:10.1038/s41467-020-14453-3.

[14] M. Higashi, T. Ozaki, Selective laser melting of pure molybdenum: evolution of defect and crystallographic texture with process parameters, Mater. Des. 191 (2020) 108588, doi:10.1016/j.matdes.2020.108588.

[15] A. Leicht, C.H. Yu, V. Luzin, U. Klement, E. Hryha, Effect of scan rotation on the microstructure development and mechanical properties of 316L parts produced by laser powder bed fusion, Mater. Charact. 163 (2020) 110309, doi:10.1016/j.matchar.2020.110309.

[16] H. Helmer, A. Bauereiß, R.F. Singer, C. Körner, Grain structure evolution in Inconel 718 during selective electron beam melting, Mater. Sci. Eng.: A 668 (2016) 180–187, doi:10.1016/j.msea.2016.05.046.

[17] R.R. Dehoff, M.M. Kirka, W.J. Sames, H. Bilheux, A.S. Tremsin, L.E. Lowe, S.S. Babu, Site specific control of crystallographic grain orientation through electron beam additive manufacturing, Mater. Sci. Technol. 31 (2015) 931–938, doi:10.1179/1743284714Y.0000000734.

[18] F. Geiger, K. Kunze, T. Etter, Tailoring the texture of IN738LC processed by selective laser melting (SLM) by specific scanning strategies, Mater. Sci. Eng.: A 661 (2016) 240–246, doi:10.1016/j.msea.2016.03.036.

[19] K.A. Sofinowski, S. Raman, X. Wang, B. Gaskey, M. Seita, Layer-wise engineering of grain orientation (LEGO) in laser powder bed fusion of stainless steel 316L, Addit. Manuf. 38 (2021) 101809, doi:10.1016/j.addma.2020.101809.

[20] A. Leicht, U. Klement, E. Hryha, Effect of build geometry on the microstructural development of 316L parts produced by additive manufacturing, Mater. Charact. 143 (2018) 137–143, doi:10.1016/j.matchar.2018.04.040.

[21] W.J. Lee, B. Weber, G. Feltrin, C. Czaderski, M. Motavalli, C. Leinenbach, Phase transformation behavior under uniaxial deformation of an Fe-Mn-Si-Cr-Ni-VC shape memory alloy, Mater. Sci. Eng.: A 581 (2013) 1–7, doi:10.1016/j.msea.2013.06.002.

[22] A. Arabi-Hashemi, X. Maeder, R. Figi, C. Schreiner, S. Griffiths, C. Leinenbach, 3D

magnetic patterning in additive manufacturing via site-specific in-situ alloy modification, Appl. Mater. Today 18 (2020) 100512, doi:10.1016/j.apmt.2019.100512.

[23] J. Günther, R. Lehnert, R. Wagner, C. Burkhardt, M. Wendler, O. Volkova, H. Biermann, T. Niendorf, Effect of Compositional Variation Induced by EBM Processing on Deformation Behavior and Phase Stability of Austenitic Cr-Mn-Ni TRIP Steel, JOM 72 (2020) 1052–1064, doi:10.1007/s11837-020-04018-6.

[24] J. Günther, F. Brenne, M. Droste, M. Wendler, O. Volkova, H. Biermann, T. Niendorf, Design of novel materials for additive manufacturing - Isotropic microstructure and high defect tolerance, Sci. Rep. 8 (2018) 1298, doi:10.1038/s41598-018-19376-0.

[25] T. Degen, M. Sadki, E. Bron, U. König, G. Nénert, The HighScore suite, Powder Diffr. 29 (2014) S13–S18, doi:10.1017/S0885715614000840.

[26] C. Haberland, M. Elahinia, J.M. Walker, H. Meier, J. Frenzel, On the development of high quality NiTi shape memory and pseudoelastic parts by additive manufacturing, Smart Mater. Struct. 23 (2014) 104002, doi:10.1088/0964-1726/23/10/104002.

[27] S. Saedi, A.S. Turabi, M. Taheri Andani, C. Haberland, H. Karaca, M. Elahinia, The influence of heat treatment on the thermomechanical response of Ni-rich NiTi alloys manufactured by selective laser melting, J. Alloys Compd. 677 (2016) 204–210, doi:10.1016/j.jallcom.2016.03.161.

[28] J. Lee, Y.C. Shin, Effects of composition and post heat treatment on shape memory characteristics and mechanical properties for laser direct deposited nitinol, Lasers Manuf. Mater. Process. 6 (2019) 41–58, doi:10.1007/s40516-019-0079-5.

[29] Q. Ren, C. Chen, Z. Lu, X. Wang, H. Lu, S. Yin, Y. Liu, H. Li, J. Wang, Z. Ren, Effect of a constant laser energy density on the evolution of microstructure and mechanical properties of NiTi shape memory alloy fabricated by laser powder bed fusion, Opt. Laser Technol. 152 (2022) 108182, doi:10.1016/j.optlastec.2022.108182.

[30] N.S. Moghaddam, S. Saedi, A. Amerinatanzi, A. Hinojos, A. Ramazani, J. Kundin, M.J. Mills, H. Karaca, M. Elahinia, Achieving superelasticity in additively manufactured NiTi in compression without post-process heat treatment, Sci. Rep. 9 (2019) 1–11.

[31] S. Griffiths, M.D. Rossell, J. Croteau, N.Q. Vo, D.C. Dunand, C. Leinenbach, Effect of laser rescanning on the grain microstructure of a selective laser melted Al-Mg-Zr alloy, Mater. Charact. 143 (2018) 34–42, doi:10.1016/j.matchar.2018.03.033.

[32] T. DebRoy, H.L. Wei, J.S. Zuback, T. Mukherjee, J.W. Elmer, J.O. Milewski, A.M. Beese, A. Wilson-Heid, A. De, W. Zhang, Additive manufacturing of metallic components – process, structure and properties, Prog. Mater. Sci. 92 (2018) 112–224, doi:10.1016/j.pmatsci.2017.10.001.

[33] J. Liu, P. Wen, Metal vaporization and its influence during laser powder bed fusion process, Mater. Des. 215 (2022) 110505, doi:10.1016/j.matdes.2022.110505.

[34] J. Zemann, Crystal structures, 2nd edition. Vol. 1 by R. W. G. Wyckoff, Acta Cryst. 18 (1965) 139–139. https://doi.org/10.1107/S0365110X65000361.

[35] N. Suutala, Effect of manganese and nitrogen on the solidification mode in austenitic stainless steel welds, Metall. Mater. Trans. A 13 (1982) 2121–2130, doi:10.1007/BF02648382.

[36] P. Köhnen, S. Ewald, J.H. Schleifenbaum, A. Belyakov, C. Haase, Controlling microstructure and mechanical properties of additively manufactured high-strength steels by tailored solidification, Addit. Manuf. 35 (2020) 101389, doi:10.1016/j.addma.2020.101389.

[37] M. Wendler, A. Weiß, L. Krüger, J. Mola, A. Franke, A. Kovalev, S. Wolf, Effect of Manganese on Microstructure and Mechanical Properties of Cast High Alloyed CrMnNi-N Steels, Adv. Eng. Mater. 15 (2013) 558–565, doi:10.1002/adem.201200318.

[38] M. Wendler, J. Mola, L. Krüger, A. Weiß, Experimental Quantification of the Austenite-Stabilizing Effect of Mn in CrMnNi As-Cast Stainless Steels, Steel Res. Int. 85 (2014) 803–810, doi:10.1002/srin.201300271.

[39] D. Kim, I. Ferretto, J.B. Jeon, C. Leinenbach, W. Lee, Formation of metastable bcc-δ phase and its transformation to fcc-γ in laser powder bed fusion of Fe–Mn–Si shape memory alloy, J. Mater. Res. Technol. 14 (2021) 2782–2788, doi:10.1016/j.jmrt.2021.08.119.

[40] M. Alnajjar, F. Christien, K. Wolski, C. Bosch, Evidence of austenite by-passing in a stainless steel obtained from laser melting additive manufacturing, Addit. Manuf. 25 (2019) 187–195, doi:10.1016/j.addma.2018.11.004.

[41] Y.M. Wang, T. Voisin, J.T. McKeown, J. Ye, N.P. Calta, Z. Li, Z. Zeng, Y. Zhang, W. Chen, T.T. Roehling, R.T. Ott, M.K. Santala, P.J. Depond, M.J. Matthews, A.V. Hamza, T. Zhu, Additively manufactured hierarchical stainless steels with high strength and ductility, Nature Mater. 17 (2018) 63–71, doi:10.1038/nmat5021.

[42] D. Borisova, C. Schimpf, A. Jahn, V. Klemm, G. Schreiber, D. Šimek, D. Rafaja, Microstructure Investigations of the Phase Boundaries in the Bridgman TRIP Steel Crystal, Solid State Phenomena 160 (2010) 211–216, doi:10.4028/www.scientific.net/SSP.160.211.

[43] E.A. Jägle, Z. Sheng, L. Wu, L. Lu, J. Risse, A. Weisheit, D. Raabe, Precipitation reactions in age-hardenable alloys during laser additive manufacturing, JOM 68 (2016) 943–949, doi:10.1007/s11837-015-1764-2.

[44] M. Ni, C. Chen, X. Wang, P. Wang, R. Li, X. Zhang, K. Zhou, Anisotropic tensile behavior of in situ precipitation strengthened Inconel 718 fabricated by additive manufacturing, Mater. Sci. Eng.: A 701 (2017) 344–351, doi:10.1016/j.msea.2017.06.098.

[45] W.J. Lee, B. Weber, G. Feltrin, C. Czaderski, M. Motavalli, C. Leinenbach, Stress recovery behaviour of an Fe–Mn–Si–Cr–Ni–VC shape memory alloy used for prestressing, Smart Mater. Struct. 22 (2013) 125037, doi:10.1088/0964-1726/22/12/125037.

[46] P.V. Muterlle, M. Zendron, M. Perina, A. Molinari, Influence of delta ferrite on mechanical properties of stainless steel produced by MIM, (n.d.) 6.

[47] K.R. Gadelrab, G. Li, M. Chiesa, T. Souier, Local characterization of austenite and ferrite phases in duplex stainless steel using MFM and nanoindentation, J. Mater. Res. 27 (2012) 1573–1579, doi:10.1557/jmr.2012.99.

[48] R.B. Figueiredo, T.G. Langdon, Effect of grain size on strength and strain rate sensitivity in metals, J. Mater. Sci. 57 (2022) 5210–5229, doi:10.1007/s10853-022-06919-0.

[49] E. Curiel-Reyna, J. Contreras, T. Rangel-Ortis, A. Herrera, L. Baños, A. del Real, M.E. Rodríguez, Effect of carbide precipitation on the structure and hardness in the heat-affected zone of hadfield steel after post-cooling treatments, Mater. Manuf. Processes 23 (2007) 14–20, doi:10.1080/10426910701524352.

[50] E.O. Hall, Variation of hardness of metals with grain size, Nature 173 (1954) 948–949, doi:10.1038/173948b0.

[51] M.J. Lai, Y.J. Li, L. Lillpopp, D. Ponge, S. Will, D. Raabe, On the origin of the improvement of shape memory effect by precipitating VC in Fe–Mn–Si-based shape memory alloys, Acta Mater. 155 (2022) 222–235 n.d..

[52] S. Kajiwara, Characteristic features of shape memory effect and related transformation behavior in Fe-based alloys, Mater. Sci. Eng.: A 273–275 (1999) 67–88, doi:10.1016/S0921-5093(99)00290-7.

[53] Y.H. Wen, M. Yan, N. Li, Effects of carbon addition and aging on the shape memory effect of Fe–Mn–Si–Cr–Ni alloys, Scr. Mater. 50 (2004) 441–444, doi:10.1016/j.scriptamat.2003.11.008.

[54] D. Rafaja, C. Ullrich, M. Motylenko, S. Martin, Microstructure aspects of the deformation mechanisms in metastable austenitic steels, in: H. Biermann, C.G. Aneziris (Eds.), Austenitic TRIP/TWIP Steels and Steel-Zirconia Composites: Design of Tough, Transformation-Strengthened Composites and Structures, Springer International Publishing, Cham, 2020, pp. 325–377, doi:10.1007/978-3-030-42603-3_11.

[55] D. Lang, Q. Li, X. Huang, W. Huang, Stacking fault energy and fcc$\rightarrow$hcp transformation driving force in Fe-Mn-C-Cr-Si high manganese steels and experimental investigation, Mater. Res. Express. 8 (2021) 086507, doi:10.1088/2053-1591/ac1c34.

[56] Q.X. Dai, X.N. Cheng, Y.T. Zhao, X.M. Luo, Z.Z. Yuan, Design of martensite transformation temperature by calculation for austenitic steels, Mater. Charact. 52 (2004) 349–354, doi:10.1016/j.matchar.2004.06.008.

[57] C. Haase, J. Bültmann, J. Hof, S. Ziegler, S. Bremen, C. Hinke, A. Schwedt, U. Prahl, W. Bleck, Exploiting process-related advantages of selective laser melting for the production of high-manganese steel, Materials (Basel) 10 (2017), doi:10.3390/ma10010056.